Journal of Umm Al-Qura University for Applied Sciences (2023) 9:529–547
https://doi.org/10.1007/s43994-023-00063-4

ORIGINAL ARTICLE

Kinetics and adsorption performance of biosorbent starch/poly(vinyl alcohol)/graphene oxide nanocomposite for the removal of dyes

V. Shanmuga Priya[1] · S. Khaleel Basha[2] · V. Sugantha Kumari[1]

Received: 31 March 2023 / Accepted: 24 June 2023 / Published online: 10 July 2023

Abstract
The present work reports an efficient removal of a cationic dye, methylene blue (MB), and an anionic dye, methyl orange (MO) dye from an aqueous solution using graphene oxide (GO)–based nanocomposite as an adsorbent. GO was investigated as a potential nano-reinforcing filler in starch/poly(vinyl alcohol) (PVA) biopolymer matrix. Bio-nanocomposite based on starch/PVA matrix and GO were prepared by an aqueous casting method. The fabricated nanocomposites were characterized using FT-IR, XRD, Raman, TEM, FE-SEM, tensile study, Brunauer–Emmett–Teller (BET) method, Barrett–Joyner–Halenda (BJH) method, zeta potential, and swelling study. The effect of the various compositions of GO nanofiller in the starch/PVA matrix was highlighted and the impact of GO nanosheets on the properties of the nanocomposites was revealed. The results demonstrated that the starch/PVA matrix with 3 g of GO was found to be the optimal concentration of GO. Batch adsorption experiments were conducted to optimize the operational factors, including adsorbent dosage, pH, and contact time, which were systematically investigated. The kinetics of adsorption followed a pseudo-second-order model, while the Langmuir isotherm model described the equilibrium adsorption capacity. The prepared nanocomposite exhibited a maximum monolayer adsorption capacity of 382 mg g^{-1} for MB dye and 293.3 mg g^{-1} for MO dye. Based on the calculated thermodynamic parameters for the adsorption of MB ($\Delta H^\circ = -16.37$ kJ mol^{-1}, $\Delta S^\circ = -37.99$ J K^{-1} mol^{-1} and ΔG° from -4.39 to -5.13 kJ mol^{-1}) and MO ($\Delta H^\circ = -13.72$ kJ mol^{-1}, $\Delta S^\circ = -31.78$ J K^{-1} mol^{-1} and ΔG° from -3.72 to -4.39 kJ mol^{-1}) dyes onto the nanocomposite material was feasible, exothermic, and spontaneous. A plausible adsorption mechanism was proposed, involving electrostatic attraction, H-bonding, and π-π interactions, which collectively governed the adsorption process. The nanocomposite showed good stability and reusability up to five cycles for the uptake of MB and MO dyes. These findings confirmed the effectiveness of the proposed approach to produce bionanocomposite with enhanced properties, which may be used in water purification technology.

Keywords Graphene oxide nanosheets · Starch · Poly(vinyl alcohol) · Nanocomposite · Dye removal

1 Introduction

Dye effluents pose significant environmental and health risks due to their genotoxic and carcinogenic nature [1, 2]. These dyes contain poorly biodegradable impurities, which not only harm the ecological environment but also have detrimental effects on human health [3, 4]. Methylene blue is a cationic dye that finds its application in color fiber, inks and highlighters, packaging materials, paints, textiles, asbestos content measurement, and paper products [5]. Methyl orange is an anionic dye used in printing, food, textile, scientific research, and pharmaceutical industries [6]. Both dyes are toxic colorants and because of their aromatic ring, degradation is difficult [7]. These dyes can cause dangerous effects such as gene mutation, cancer, and skin allergies [8, 9]. To address these issues and create a safer environment, various techniques have been proposed for dye removal, including photocatalysis [10, 11], biological treatment [12], chemical oxidation [13], membrane separation [14], and adsorption [15]. Among these methods, adsorption stands out as an inexpensive, easy-to-perform, and efficient technique for dye removal [16].

✉ V. Sugantha Kumari
suganthak@auxiliumcollege.edu.in

[1] PG and Research Department of Chemistry, Auxilium College (Autonomous), (Affiliated to Thiruvalluvar University, Serkkadu), Vellore 632006, Tamil Nadu, India

[2] PG and Research Department of Chemistry, C. Abdul Hakeem College, Melvisharam 632509, Tamil Nadu, India

Materials with ease in availability and low cost are preferred for this purpose. In this context, starch is considered a significant material for adsorption. Starch, a low-cost, abundant, renewable, and biodegradable natural polymer, has been widely used to construct effective composites with GO [17]. However, the poor mechanical properties of starch have limited its applicability. To enhance its characteristics, starch is often combined with other compounds, such as biodegradable synthetic polymer polyvinyl alcohol (PVA) [18]. PVA, known for its non-toxicity, water solubility, and good chemical and thermal stability, provides a biocompatible microenvironment when combined with starch. The use of starch and PVA in the nanocomposite formulation aligns with sustainability goals and reduces the reliance on non-renewable resources [19, 20]. The incorporation of starch and PVA into the Graphene oxide based-nanocomposite can improve the overall performance of the material.

Carbon-based nanomaterials, such as graphene oxide (GO), have gained attention as superior adsorbents in aqueous solutions for isolating organic dye pollutants [21]. GO is an oxygen-rich carbonaceous material with excellent mechanical properties and a large specific surface area, making it suitable for environmental remediation without interfering with ecological processes [22]. As it is well known, GO is synthesized dominantly via the chemical oxidation of natural graphite even though there are few reports on alternative electrochemical oxidation [23]. One commonly used method for synthesizing graphene oxide is the modified Hummers method [24], which is an adaptation of the original Hummers method [25]. This method enables better control over the degree of oxidation and enhances the efficiency in producing graphene oxide with functional groups on its surface. The oxidation process introduces various functional moieties, such as hydroxyl (–OH), carboxyl (–COOH), and ether (–C–O–C) groups, onto the graphitic layers of GO [26, 27]. These functional groups act as active sites for efficiently removing dye contaminants from aqueous environments. Recently, there has been growing interest in GO-based nanocomposites, which offer the ability to tailor their properties for specific applications [28]. GO, as a reinforcing filler, can be incorporated into the composite by various supramolecular interactions including hydrogen bonding, electrostatic interaction, coordination, and π–π stacking. The extended layered structure of GO with large surface area and hydrophilic polar groups can increase swelling property, mechanical strength, and adsorption ability of the nanocomposite [29]. GO-based nanocomposites with good dispersion and interfacial bonding can prevent the aggregation of GO nanosheets, leading to composites with superior properties compared to their individual components [30, 31].

Research in the field of adsorption has predominantly focused on investigating the isotherm, kinetic, and thermodynamic aspects of the adsorption process to gain insights into the mechanism by which dye molecules are adsorbed onto different adsorbents. According to the literature, to explore the appropriate adsorbent, several notable studies have been published in this regard. Alamri et al. successfully grafted thiol (–SH) and sulfonic acid ($–SO_3H$) groups onto Titanosilicate (TS) for dioxane cleanup. These adsorbents well obeyed the Langmuir adsorption isotherm and pseudo-second order model when removing dioxane from polluted environments [32]. Fakhry et al. used phase inversion technique to immobilized *Myriophyllum spicatum* L. onto polyacrylonitrile/polyvinylpyrrolidone (PAN/PVP) hybrid beads, resulting in a porous structure with a positive impact from PVP incorporation. The fabricated beads exhibited high adsorption capacity (217 mg g^{-1}) for Safranin O dye, following the Langmuir isotherm model, and showed promising reusability, making them suitable for cost-effective wastewater treatment in the textile industry [33]. Nassar et al. presented the synthesis of pure sphere-like spinel $CoMn_2O_4$ nanostructures and their application as an adsorbent for the removal of Reactive Black 5 dye from aqueous solutions [34]. The synthesized adsorbent exhibits high adsorption capacity, stability, and reusability, and follows pseudo-second-order kinetics and Langmuir isotherm model for adsorption.

Herein, we introduce GO as a nanofiller in the starch/PVA polymer matrix to prevent the aggregation of GO and fully exploit its adsorption capabilities. We assess the adsorption performance of the starch/PVA/GO (SPGO) nanocomposite for the removal of the cationic dye MB and the anionic dye MO from aqueous solutions. The Langmuir and Freundlich adsorption models were used to describe the equilibrium isotherm. Two simplified kinetic models including pseudo-first-order and pseudo-second-order equations were used to investigate the adsorption process. The novel aspect of our study lies in investigating the adsorption potential of the SPGO nanocomposite, which combines the advantages of GO, starch, and PVA, offering a promising solution for effective dye removal.

2 Materials and methods

2.1 Materials

Graphite powder, sodium nitrate ($NaNO_3$), sulphuric acid (H_2SO_4), potassium permanganate ($KMnO_4$), 30% hydrogen peroxide (H_2O_2), hydrochloric acid (HCl) and ethanol was supplied by Sigma-Aldrich. Starch (MW = 828.718) and Polyvinyl alcohol (MW = 85,000–124,000 g mol^{-1} with 88% of degree of hydrolysis) was purchased from Spectrochemicals Pvt Ltd., Mumbai, India. Dye for adsorption studies including methylene blue (MB, $C_{16}H_{18}ClN_3S$) and methyl orange (MO, $C_{14}H_{14}N_3NaO_3S$) was supplied by Sigma-Aldrich). All

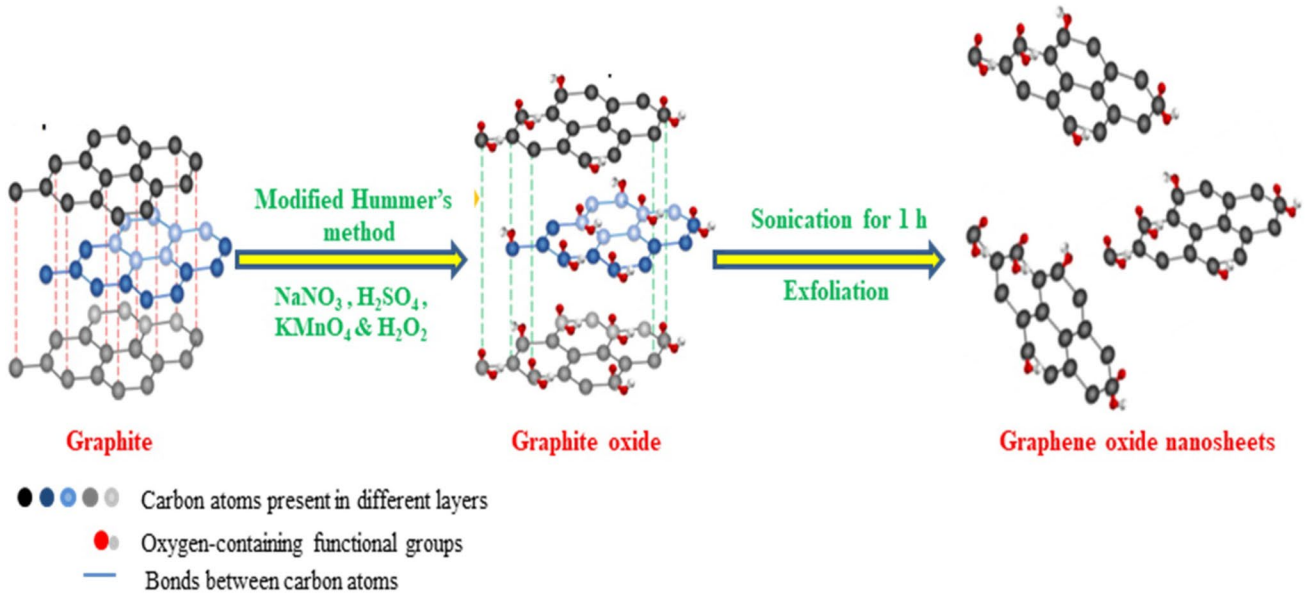

Scheme 1. Synthesis of graphene oxide nanosheet

aqueous solutions were prepared with de-ionized water (DI water). All chemicals used were of analytical grade.

2.2 Synthesis of graphene oxide nanosheets (GO)

Graphene oxide (GO) was synthesized by a modified Hummers method [24]. Sulfuric acid was mixed with phosphoric acid with a 9:1 volume ratio, the mixture was stirred for 10 min. Graphite powder was then added to the mixture while stirring. Potassium permanganate was slowly added to the solution mixture and left to stir for 6 h until the color changed to dark green. 0.675 mL of hydrogen peroxide was slowly added producing an exothermic reaction and the reaction was left to stir for several minutes. The reaction temperature was lowered to room temperature (~25 °C) and then the solution was centrifuged and the precipitate was washed by a mixture of HCl and distilled water several times. The produced GO powder was set to dry in a drying oven at 90 °C for 24 h (Scheme 1).

2.3 Fabrication of starch/poly(vinyl alcohol)/graphene oxide nanocomposite (SPGO)

The fabrication of GO-based nanocomposite containing starch and PVA was prepared by the solution casting method [17, 19]. Starch (2 g) was dissolved in 100 mL deionized water and stirred for 1 h at 95 °C to induce starch gelatinization. PVA (2 g) was prepared in 100 mL deionized water and stirred for 1 h at 90 °C. Then the starch solution and the PVA solution were mixed in the volume ratio of 3:1 and stirred for 1 h at room temperature followed by sonication for 30 min. To 100 mL starch/PVA blend solution, various proportions of GO nanofiller (1 g, 3 g, and 5 g) were added individually followed by sonication for 2 h. The obtained homogenous dispersions were cast onto Teflon plates and dried at 35 °C for approximately 72 h. While using Teflon plate additional processing steps have been carried out including sonication for 1 h additionally in the same conditions and complete drying for at least 1 week prior to the demolding process to produce bubble-free materials and further ensure proper bonding between the nanocomposites. The dried nanocomposites were peeled from the casting surface and kept in a desiccator at room temperature until further use. The samples were coded as SPGO0 (polymer matrix) and the nanocomposites with GO (1 g, 3 g, and 5 g) as SPGO1, SPGO3, and SPGO5 respectively (Scheme 2).

2.4 Characterizations of starch/poly(vinyl alcohol)/graphene oxide nanocomposite

2.4.1 Fourier transform infrared spectroscopy (FTIR)

Fourier-transform infrared spectrometer (FTIR, Nicolet-560) (USA) was used to characterize the chemical structure of the prepared materials. Each transmission mode was developed with a resolution of 4 cm^{-1} and a range of 4000–400 cm^{-1}.

2.4.2 X-ray diffraction analysis (XRD)

An X-ray diffractometer (SmartLab, Rigaku Corporation International Marketing Division, Japan) was used to analyze the diffraction patterns of the prepared materials.

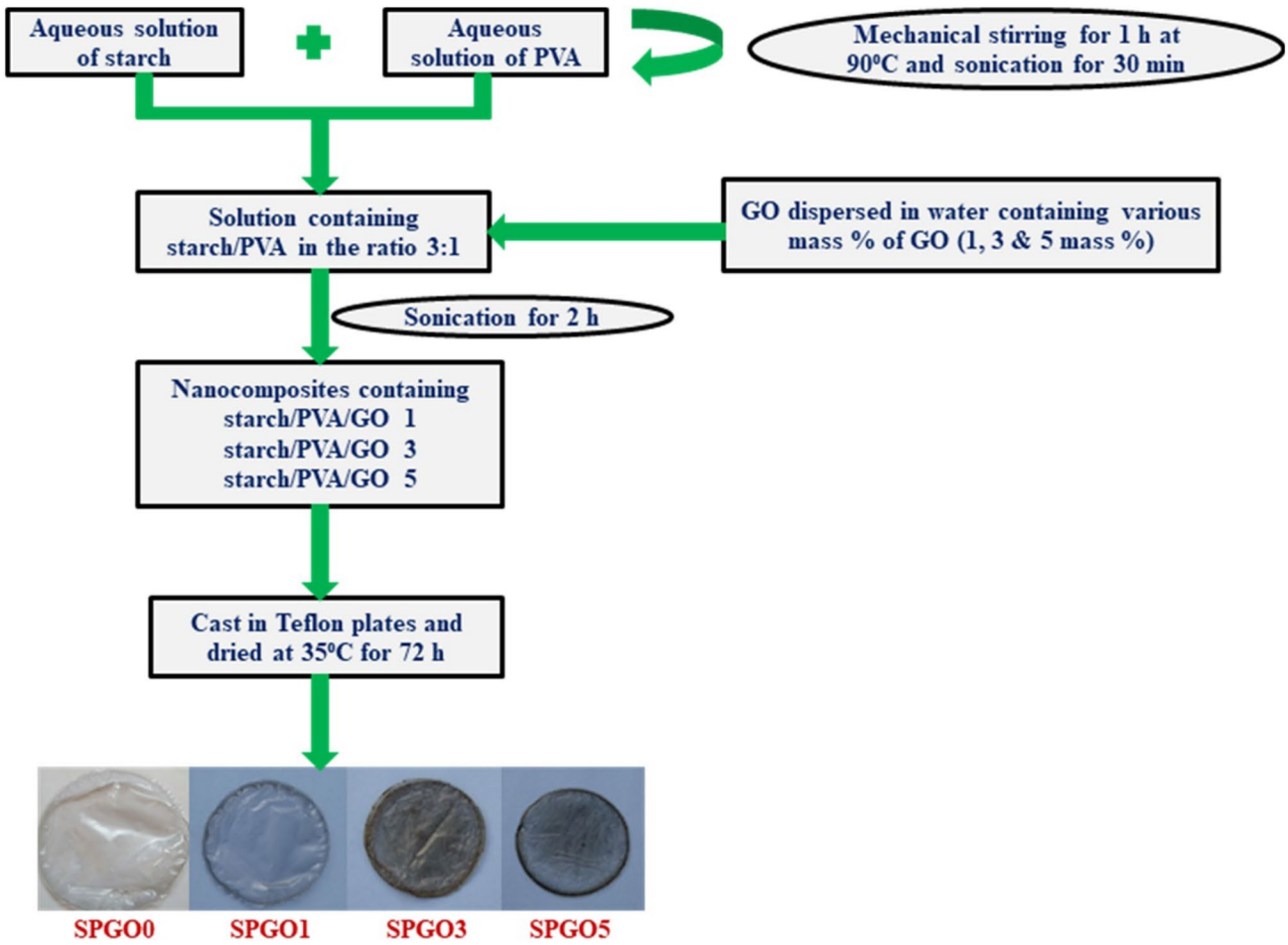

Scheme 2. Fabrication of starch/poly(vinyl alcohol)/graphene oxide nanocomposite (SPGO)

XRD graphs were recorded at a 20° min^{-1} scanning speed in $10° \leq 2\theta \leq 90°$ intervals for qualitative analysis. The wavelength of CuKα radiation was 1.540 Å. The d-spacing was evaluated by Bragg's law [35]:

$$d = \frac{n\lambda}{2sin\theta} \quad (1)$$

where n is the order of reflection, λ is the wavelength of the X-ray, d is the characteristic spacing between crystal planes of a given specimen and θ is the angle formed between the incident beam and that of the normal to the lattice plane.

2.4.3 Raman spectroscopy

Confocal Raman Spectroscopy/Imaging, Alpha300R, WITec GmbH Germany, was used to study the structural defects of the prepared materials at an excitation wavelength of 532 nm.

2.4.4 Transmission electron microscopy (TEM)

Transmission electron microscope (TEM) (model Philips CM 200) was used to investigate the morphology of graphite powder and graphene oxide nanosheets (GO). A droplet of diluted suspension of graphite and GO were deposited on the surface of a clean copper grid and dried at room temperature.

2.4.5 Field emission scanning electron microscopy (FE-SEM)

A field emission scanning electron microscope (FESEM), Quattro S, FEI Company of USA (S.E.A) PTE LTD, Singapore, was used to examine the surface morphology of the prepared materials.

2.4.6 Mechanical study

Mechanical properties such as tensile strength (TS) and percentage of elongation at break (EB) were carried out for the as-prepared materials using MTS Criterion 5 kN testing Machine according to ASTM D-638-2010 with a crosshead speed of 50 mm min^{-1}. The measurements were done at 25 °C. Sample dimensions were 4 mm × 10 mm. This experiment was performed in triplicates and data were expressed as the means of triplicate counts.

2.4.7 BET analysis

The Brunauer–Emmett–Teller (BET) specific surface area and Barrett–Joyner–Halenda (BJH) pore volume of the material were determined based on N_2 adsorption–desorption tests performed by BET Surface area analyzer, BELSorp Max, Microtrac, BEL Corp, Japan.

2.4.8 Zeta potential

The surface charge of the prepared materials was determined using Zeta potential analyzer, Microtrac, Inc., USA, under varying pH.

2.4.9 Swelling study

The equilibrium swelling behavior of the prepared materials was evaluated by immersing a known weight of the material in DI water at pH 7. The materials were equilibrated in an incubator shaker at 37 °C and taken out from the solution after 24 h. The excess surface water was removed using a wet filter paper to obtain the weight of swollen material (W_w). The prepared materials were then dried overnight in an oven at 60 °C and the dry weight (W_d) was determined. The swelling ratio was determined according to the equation [36]:

$$\text{Swelling ratio}(\%) = \frac{W_w - W_d}{W_d} \times 100\% \quad (2)$$

2.5 Adsorption study

Batch adsorption experiments were carried out in conical flasks, where SPGO3 (1–8 mg dosage for MB and 1–4 mg dosage for MO) was added to 25 mL of dye the solution (5–300 mg L^{-1} for MB and 10–200 mg L^{-1} for MO) at pH ranging from 3 to 11. The pH values of the solutions were adjusted by adding 0.1 M HCl and 0.1 M NaOH solutions. The solutions were agitated under 150 rpm in a temperature-controlled shaker at 298, 308 and 318 K. The adsorption kinetic experiments were studied at various time intervals from 10 to 180 min. The concentration of dye at different time intervals was determined by UV–Vis spectrometer (JAZ, Ocean optics, USA) by measuring their absorbance at λ_{max} of MB (664 nm) and MO (464 nm). Adsorption capacity (q_e) and removal efficiency (R) were calculated using the following equations:

$$q_e = \frac{(C_0 - C_e)V}{m} \quad (3)$$

$$R = \frac{C_0 - C_e}{C_0} \times 100\% \quad (4)$$

where qe is the adsorption capacity (mg g^{-1}), C_0 and C_e are the initial and equilibrium concentrations of selected dyes (mg L^{-1}), respectively, V is the volume of the solution (L), and m is the mass of the adsorbent (g).

To investigate the effect of ionic strength, a series of solutions with varying concentrations of KCl, NaCl, $CaCl_2$, and $MgCl_2$ were added to the flask containing adsorbent (6 mg dosage for MB and 10 mg dosage for MO) and adsorbate (V = 25 mL, C = 30 mg L^{-1} for MB and MO dyes) at 298 K.

2.6 Reusability studies

After adsorption of dyes, to separate the dye-loaded SPGO3 nanocomposite, 0.1 M HCl solution was used as a desorption medium for MB, and 0.1 M NaOH solution was used as a desorption medium for MO. After centrifugation, the separated SPGO3 nanocomposite was then washed with water and ethanol, in sequence. The nanocomposite was then dried at 35 °C for 72 h and used for the subsequent adsorption–desorption experiments. The desorbed dye concentrations were quantified by UV–visible spectroscopy. The adsorption capacity (q_e) of SPGO3 nanocomposite was calculated using Eq. (3).

2.7 Statistical analysis

Each batch adsorption experiment was performed thrice and the obtained results were presented as average ± SD (standard deviation). The maximum errors were less than 5%.

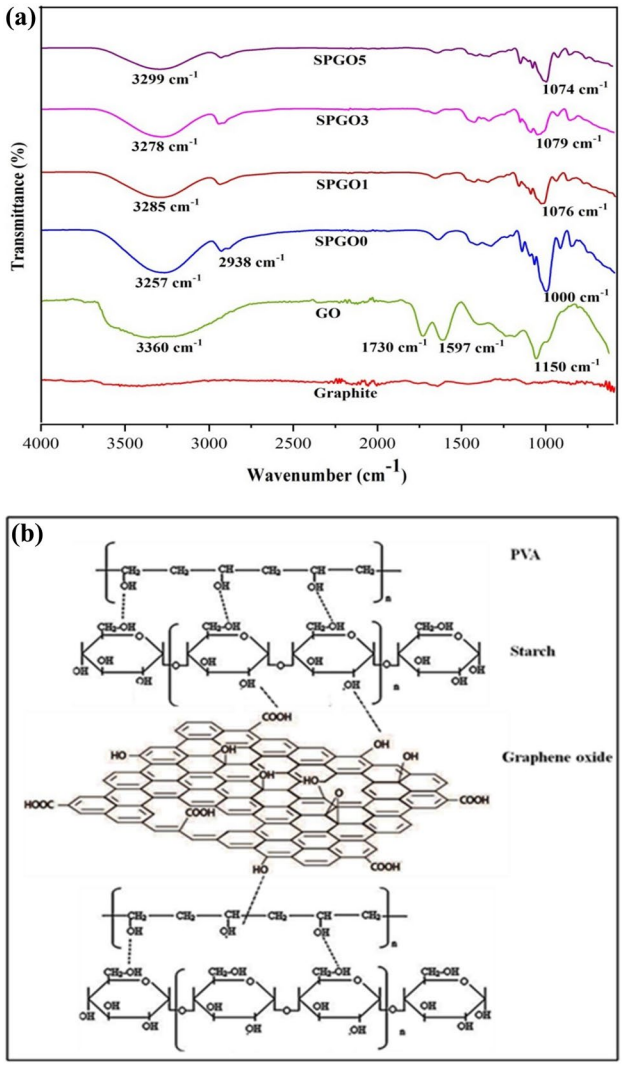

Fig. 1 **a** FTIR spectra of Graphite, GO, SPGO0 polymer matrix and SPGO nanocomposites and **b** Intermolecular hydrogen bonding existed in SPGO nanocomposites

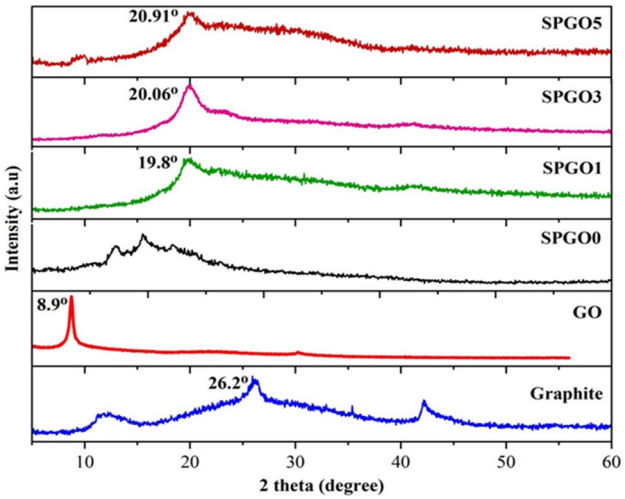

Fig. 2 XRD pattern of Graphite, GO and SPGO nanocomposites

3 Results and discussion

3.1 Characterizations of starch/poly(vinyl alcohol)/graphene oxide nanocomposite

3.1.1 Fourier transform infrared spectroscopy (FT-IR)

The functional groups and chemical bonding in graphite, pristine GO, SPGO0 polymer blend, and SPGO1, SPGO3, and SPGO5 nanocomposites were validated by FT-IR spectroscopy as shown in Fig. 1a. The findings showed that while GO supported the existence of diverse oxygen-containing functional groups on its surface, graphite did not show typical peaks of functional groups on its surface. This demonstrated that the conversion of graphite to GO was successful. The stretching vibration of –OH was represented by a distinctive broadband in the GO spectra, located at approximately 3360 cm^{-1} [37, 38]. The stretching vibrations of C=O, aromatic C=C, C–O–C, and C–O were assigned to the absorption bands at 1730 cm^{-1}, 1597 cm^{-1}, 1250 cm^{-1}, and 1150 cm^{-1}, respectively [39]. These vibrations revealed the characteristic signatures of oxygen-containing functional groups on the GO surface. The presence of functional groups in GO promotes its hydrophilic character and facilitates its dispersion in water [40]. This property plays an important role in the adsorption of dyes and heavy metals from an aqueous solution. The distinctive peak for the SPGO0 polymer blend at 3257 cm^{-1} and 2938 cm^{-1} corresponds to the stretching vibrations of –OH and $–CH_2$, respectively. Between 1330 cm^{-1} and 1000 cm^{-1}, the stretching vibrations of the C–O in the C–O–H and C–O–C groups were noticed. This confirmed strong interaction and miscibility between starch/PVA polymer matrix. In SPGO1, SPGO3, and SPGO5 nanocomposites, the –OH stretching frequency in GO decreased from 3360 cm^{-1} to 3285 cm^{-1}, 3278 cm^{-1}, and 3299 cm^{-1}, respectively. The intermolecular hydrogen bonding between the GO nanofiller and the starch/PVA polymer matrix was responsible for the shift in the –OH band to a lower vibrational frequency (Fig. 1b). This association increases the molecular level dispersion of GO nanofiller in the starch/PVA polymer matrix. Additionally, in SPGO1, SPGO3, and SPGO5 nanocomposites, the C–O stretching frequency in GO was changed from 1150 cm^{-1} to 1076 cm^{-1}, 1079 cm^{-1}, and 1074 cm^{-1}, respectively. The changes in the spectra of SPGO nanocomposites to GO suggested the presence of strong interactions between GO nanofiller and starch/PVA polymer matrix.

3.1.2 X-ray diffraction (XRD)

To study the degree of exfoliation, interlayer distance (evaluated by Bragg's law), and dispersion of GO in the SPGO nanocomposites, X-ray diffraction analysis was performed and the results were shown in Fig. 2. The diffraction pattern of the graphite revealed a single sharp peak at $2\theta = 26.2°$ corresponding to the indices of (002) plane of highly organized layer structure exhibiting an interlayer spacing of 0.34 nm. The diffraction peak detected at $2\theta = 8.9°$ could be attributed to GO displaying an interlayer spacing of 0.99 nm. The increase in the interlayer spacing of GO when compared to graphite might be attributed to the oxidation of graphite to GO, where the oxidation intercalates abundant oxygen-containing functional groups in the interlayer of graphite [40]. The increased interlayer distance in GO nanosheets was also correlated with the enhancement in the adsorption behavior of SPGO nanocomposites.

The diffraction pattern of the SPGO nanocomposites clearly explained that the degree of dispersion varied with the amount of incorporation of GO nanosheets in the starch/PVA matrix. In the SPGO0 polymer blend, the crystallinity of PVA decreased on blending with starch. This indicated that strong interaction exists due to the hydrogen bonding between the hydroxyl groups of starch and PVA [19]. In SPGO1, SPGO3 and SPGO5 nanocomposites characteristic peaks appeared around 19.8°, 20.06°, and 20.91° with d-spacing 0.45, 0.44, and 0.42 nm, respectively. The absence of characteristic diffraction peak of GO in SPGO1 and SPGO3 indicated that most of the GO nanosheets were dispersed homogeneously within the polymer matrix. This could be related to the intermolecular hydrogen bonding in the nanocomposites, confirmed by FT-IR. But in SPGO5 nanocomposite, the characteristic peak of GO reappeared, but with less intensity. This could be attributed to the layer stacking of GO sheets in the starch/PVA matrix which leads to poor dispersion [35]. The stacking of GO sheets directly affected the nanocomposite property which was reflected in tensile strength results. Hence XRD result showed good compatibility and optimal dispersibility with SPGO3 nanocomposite.

3.1.3 Raman spectroscopy

The structural information of Graphite, pristine GO, SPGO1, SPGO3, and SPGO5 nanocomposites were obtained using Raman spectroscopic technique, shown in Fig. 3. The Raman spectra of graphite, GO, and SPGO nanocomposites exhibited characteristic D and G bands at approximately 1350 cm^{-1} and 1580 cm^{-1} respectively. The D band was associated with the stretching vibration of sp^3 carbon atoms causing defects and disorder of GO, while the G band was due to the stretching vibration of sp^2 carbon atoms in a

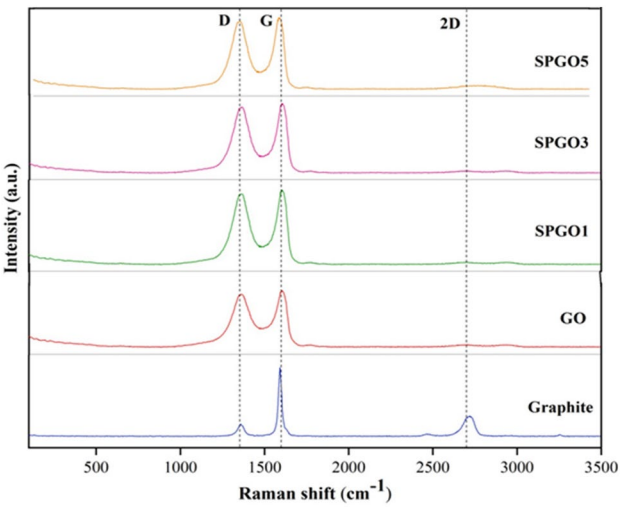

Fig. 3 Raman spectra of Graphite, GO and SPGO nanocomposites

graphitic 2D hexagonal lattice [41]. It was observed that the D band of GO was broader and more intense than graphite, which indicated that symmetry was distorted in GO because of the introduction of functional groups. Therefore, the defects caused in GO were due to the presence of functional groups on the surface of GO. The relative intensities of the D and G bands (I_D/I_G) could be correlated to the ratio between the sp^3 and sp^2 carbon atoms and therefore used to estimate the defects in the graphene layers [42]. The increase in I_D/I_G ratio from 0.08 for graphite to 0.9 for GO served as a measure of disorder and inclusion of oxygen-containing functional groups within the carbon–carbon lattice.

The successful incorporation of GO nanosheets in the starch/PVA matrix was confirmed by the I_D/I_G ratio of SPGO nanocomposites. The I_D/I_G ratio was slightly enhanced in all the SPGO nanocomposites compared with that of GO, indicating more structural defects of GO sheets [43] due to the formation of chemical bonds between GO and starch/PVA matrix. Graphite revealed an intense 2D peak due to its layered structure. It was noticed that in the spectra of GO and SPGO nanocomposites, the 2D bands were single broad peaks indexed around 2700 cm^{-1}, except graphite. The number of layers of graphene sheets and their relative orientations affect the 2D band. In the case of SPGO5 nanocomposite, a wider 2D band suggested that aggregation in several layers of graphene oxide occurred [44].

3.1.4 Transmission electron microscopy (TEM)

TEM images provide direct evidence for the morphology and degree of exfoliation of graphite and GO which were shown in Fig. 4. Tightly stacked layered structure of the graphitized framework was clearly observed in the high-magnification image of raw graphite (Fig. 4a).

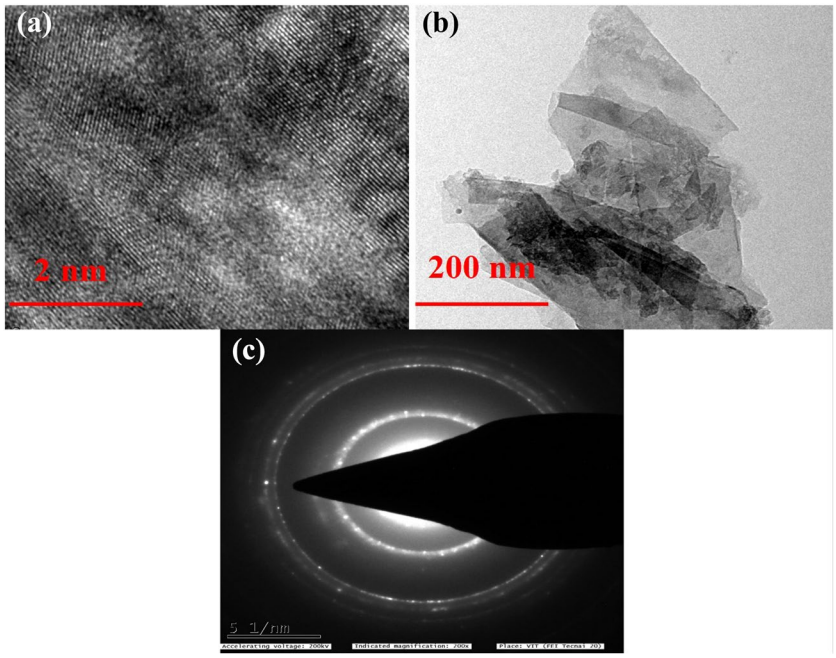

Fig. 4 TEM micrographs of **a** graphite powder, **b** GO nanosheets and **c** SAED pattern of GO nanosheets

After oxidation, the obtained GO nanosheets appeared to be transparent giving sheet-like morphology with distinct folding. This indicated that a high degree of exfoliation was achieved. Good transparency also suggested the presence of few-layered GO (Fig. 4b). The selected-area electron diffraction (SAED) (Fig. 4c) of GO showed two visible concentric rings. The first ring corresponds to (1100) plane and the second corresponds to (1120) plane [39], which could be explained by the presence of functional groups on the surface of GO that modified the diffraction pattern.

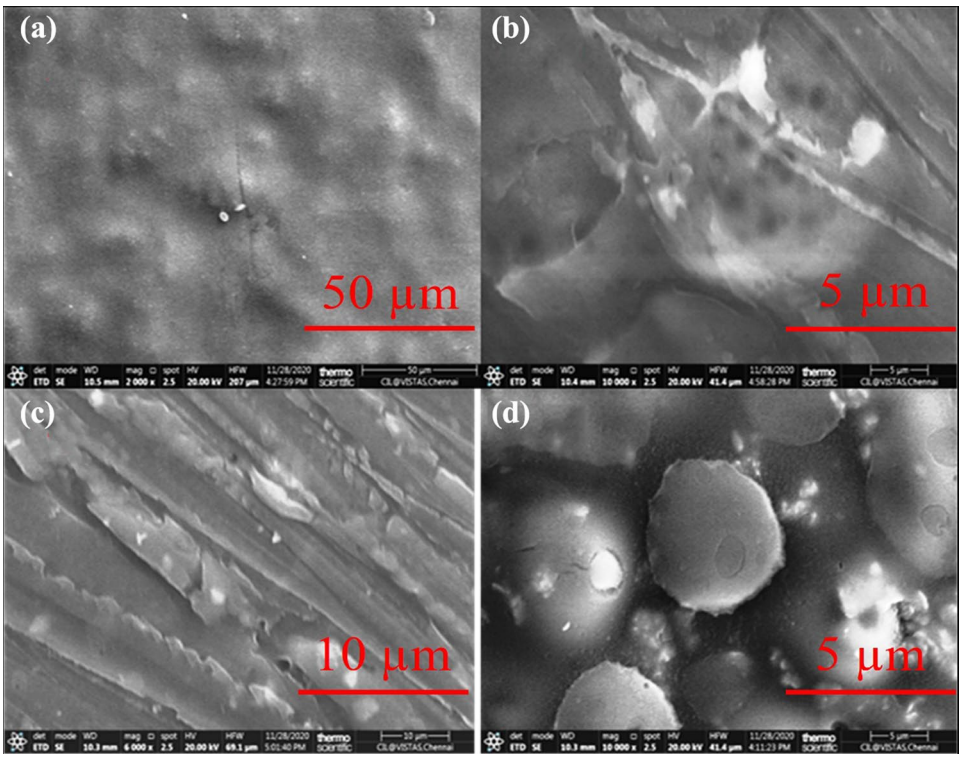

Fig. 5 FE-SEM images of **a** SPGO0 polymer matrix, **b** SPGO1, **c** SPGO3 and **d** SPGO5 nanocomposites

3.1.5 Field emission scanning electron microscopy (FESEM)

FESEM analysis was performed to study the surface morphology of SPGO0 polymer blend, SPGO1, SPGO3, and SPGO5 nanocomposites and the corresponding micrographs were represented in Fig. 5a–d. The SPGO0 blend showed a smooth and homogeneous morphology, suggesting a homogeneous phase construction through strong inter- and intra-molecular hydrogen bonding. After the addition of GO nanofiller, the differences in the morphology of SPGO1, SPGO3, and SPGO5 nanocomposites were explained by the hydrophilic functional groups of GO which facilitate a strong interaction and better dispersion between the GO nanofiller and starch/PVA polymer matrix. In the case of SPGO5 nanocomposite, a few agglomerations were observed due to the tendency of GO to agglomerate at higher concentrations [45]. In addition, FESEM images of all SPGO nanocomposites showed a rough surface after the incorporation of GO. The GO nanofiller provides active adsorption sites in SPGO material which significantly attract more target pollutants and accordingly improved the rate of adsorption and adsorption capacities in theory [46].

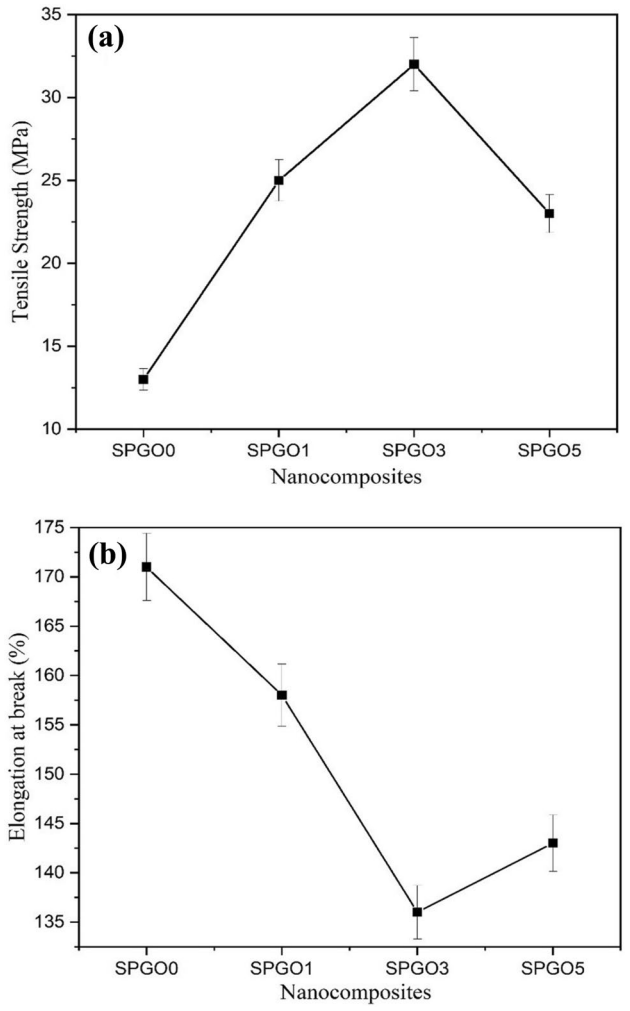

Fig. 6 **a** Tensile strength of SPGO0 polymer matrix and SPGO nanocomposites and **b** elongation at break of SPGO0 polymer and SPGO nanocomposites

3.1.6 Mechanical property

Mechanical properties such as tensile strength (TS) and percentage elongation at break (EB %) of SPGO0, SPGO1, SPGO3, and SPGO5 nanocomposites were tested and the results are shown in Fig. 6a, b. A good adsorbent must be mechanically stable when handling. SPGO0 polymer blend showed higher EB and lower TS. The increase in TS of SPGO1, SPGO3, and SPGO5 exhibited the reinforcing effect of GO nanosheets. This could be due to the formation of a more bonded network that was generated by the addition of GO nanosheets within the starch/PVA matrix [40]. The TS of SPGO3 increased as compared to SPGO1 due to greater integration of GO nanosheets with the starch/PVA polymer matrix. The homogeneous dispersion of GO nanosheets in the starch/PVA matrix, as well as favourable interfacial interactions, contributed to the enhanced TS of SPGO3 nanocomposite. Because of the greater concentration of GO in SPGO5, TS decreased due to the aggregation of GO nanosheets [35]. The incorporation of GO nanosheets, on the other hand, decreased the EB by limiting the nanocomposite's elongation by producing a stronger network in the starch/PVA matrix [47]. According to the findings, good mechanical integrity was obtained with SPGO3.

3.1.7 BET analysis

The N_2 adsorption–desorption isotherms were employed and the corresponding pore size distribution curves obtained using the BJH method are shown in Fig. 7a, b, respectively. The isotherm belonged to type IV and the hysteresis loop indicated that SPGO3 possessed the presence of mesopores [48]. The estimated mesopore size for SPGO3 nanocomposite was 3.5. nm, as shown in Fig. 7b, demonstrating a homogeneous pore size distribution. The BET specific surface area of SPGO3 nanocomposite was found to be 96.6 $m^2\ g^{-1}$. The calculated surface area was attributed to the presence of GO nanosheets in the material. The high specific surface area and mesoporous feature of SPGO3 nanocomposite, therefore, provided more adsorption sites.

3.1.8 Zeta potential

The surface charges of pure GO and SPGO3 nanocomposite were determined as zeta potential of the nanocomposite for the pH range of 2–12 and the results are shown in Fig. 8. The results from the figure explained that the

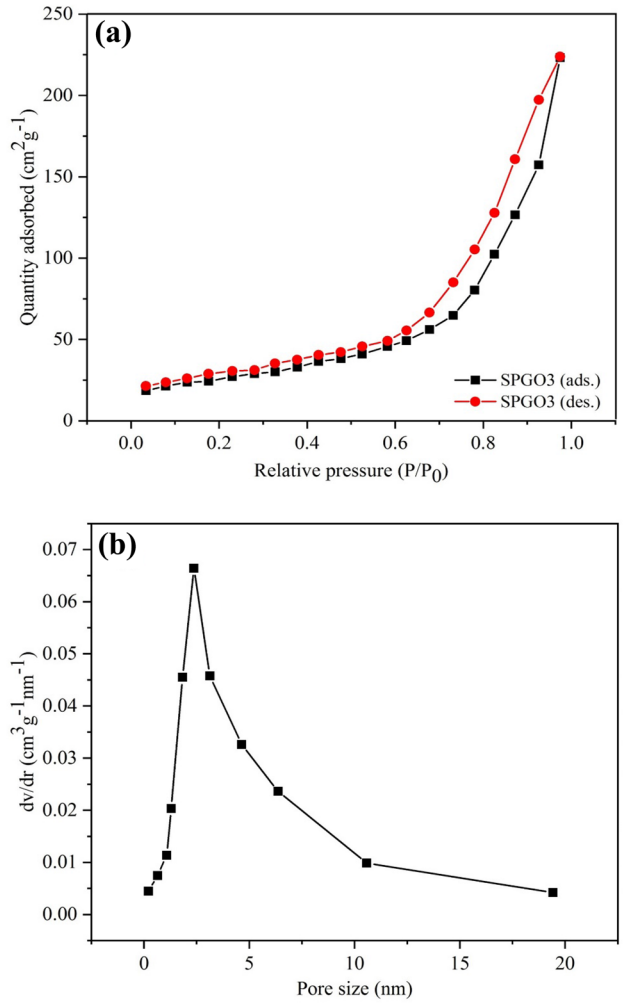

Fig. 7 **a** N_2 adsorption–desorption isotherms of SPGO3 nanocomposite and **b** pore size distributions of SPGO3 nanocomposite

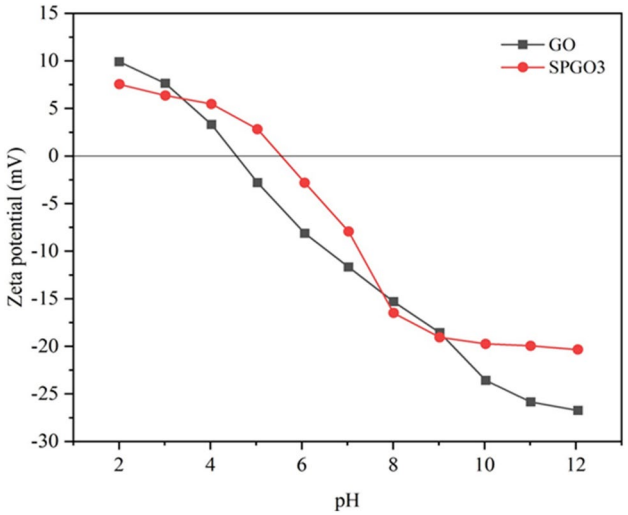

Fig. 8 Zeta potential of GO and SPGO3 nanocomposite at different pH

surface charge of the adsorbent was affected to a great extent by the solution pH. The SPGO3 nanocomposite exhibited high densities of negative charge compared to pure GO in alkaline pH. This was ascribed to the presence of oxygen-containing functional groups of GO and the hydroxyl groups on the polymeric chain, making the surface of SPGO3 negatively charged in alkaline pH. The point of zero charge (pH_{pzc}) is the pH at which the surface charge of the adsorbent becomes zero. It is negatively charged at $pH > pH_{pzc}$ and positively charged at $pH < pH_{pzc}$ [31]. This study showed that $pH_{pzc} = 5.8$ for SPGO3 and $pH_{pzc} = 4.5$ for GO. From the zeta potential analysis, it was expected that the negative surface charge of SPGO3 will be favorable for electrostatic attraction with that of the pollutant. Hence the zeta potential values to the pH will be useful in establishing a plausible adsorption mechanism.

3.1.9 Swelling study

The tendency of a nanocomposite to swell is a critical aspect in determining its suitability for adsorption applications. The swelling capacity of the SPGO0 blend and the formulated SPGO nanocomposites were shown in Table 1. The water uptake nature is mainly due to the presence of hydrophilic groups such as hydroxylic (–OH), carboxylic (–COOH), etc. which are present in the nanocomposite network [49]. The greater the number of hydrophilic groups in a nanocomposite, the greater the swelling. The hydrophilic functional groups of GO, starch, and PVA were involved in the swelling of SPGO nanocomposites. In SPGO0 (devoid of GO nanofiller), the swelling ratio was found to be 238%. When GO was introduced into SPGO1, SPGO3 and SPGO5 nanocomposites, the swelling ratio was increased to 994%, 1086% and 903%, respectively. The greater swelling ability in nanocomposite was attributed to the better quantity and availability of polar functional groups contributed by the GO nanofiller. The sample with the highest degree of swelling will have the highest surface area/volume ratio [50]. The higher swelling capacity of SPGO3 nanocomposite may be related to the more hydrophilic nature of this material.

Table 1 Swelling study

Nanocomposite	Swelling ratio (%)
SPGO0	237
SPGO1	994
SPGO3	1086
SPGO5	903

3.2 Optimization of operational factors on the adsorption

The amount of GO loadings anchored on the surface of the starch/PVA matrix plays an important role in determining the property of an adsorbent. From the characterization techniques, it was observed that GO tends to agglomerate at higher concentrations. This tendency reduces the accessibility of adsorption sites on GO. The SPGO3 nanocomposite showed optimal dispersibility of GO nanofiller and also due to the presence of GO component endowed the SPGO3 nanocomposite with a large surface area. Therefore, we chose SPGO3 nanocomposite as the nano adsorbent to further investigate the removal of dye pollutants from an aqueous solution. Methylene blue (MB) and methyl orange (MO) were chosen as model organic dyes.

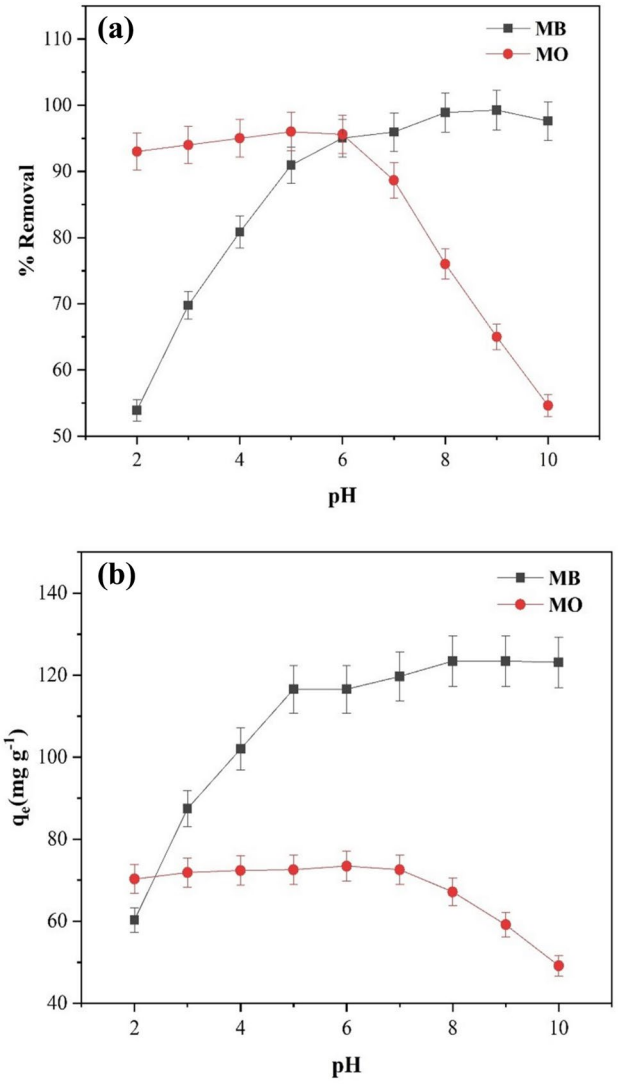

Fig. 9 Effect of pH on **a** Removal of MB and MO dye by SPGO3 nanocomposite and **b** Adsorption capacity for SPGO3 nanocomposite (c_0 = 30 mg L^{-1}; V = 25 mL; temperature was 298 K). Error bar = SD (n = 2)

3.2.1 Effect of pH

The pH level plays a crucial role in influencing the protonation of functional groups and, consequently, the surface potential of the SPGO3 nanocomposite [51]. To investigate the impact of pH on the removal efficiency and adsorption capacity of the SPGO3 nanocomposite, the experiments was conducted and presented the results in Fig. 9a, b. Additionally, the effect of pH can be understood by considering the point of zero charge (pH_{pzc}) value, which was determined through zeta potential measurements [31]. From Fig. 8, the pH_{pzc} of the SPGO3 nanocomposite was found to be 5.8. Below pH 5.8, the surface of SPGO3 carried a positive charge, while above pH 5.8, the surface of SPGO3 exhibited a negative charge. In aqueous solutions, the dyes methylene blue (MB) and methyl orange (MO) existed in cationic and anionic forms, respectively. From Fig. 9a, b, it was clear that the highest removal efficiency (98%) for MB was achieved at a solution pH of 8. On the other hand, increasing the pH beyond this point did not lead to a further increase in adsorption capacity. This observation suggests that as the solution pH gradually increased, the hydroxyl and carboxyl functional groups on SPGO3 became deprotonated. Consequently, cationic MB molecules were able to bind to the negatively charged surface of the SPGO3 nanocomposite through electrostatic attraction. Therefore, the negative surface charge of the adsorbent played a significant role in the removal of MB dye. For the anionic dye, MO, the maximum removal efficiency (94%) was attained at a solution pH of 5. Similar to MB, increasing the pH beyond this point did not enhance the adsorption capacity. This finding indicates that at lower pH levels, the functional groups on SPGO3 were protonated, which increased the adsorption of the anionic dye. Thus, pH 8 and pH 5 were determined as the optimum pH values for the adsorption of MB and MO, respectively, in all subsequent experiments.

3.2.2 Effect of adsorbent dosage

The effect of adsorbent dosage on MB and MO removal by SPGO3 nanocomposite was investigated and its influence on removal efficiency and adsorption capacity are shown in Fig. 10a, b, respectively. It was observed that adsorption capacity decreased significantly by increasing the adsorption dosage from 1 to 14 mg which may be attributed to the splitting effect of flux or concentration gradient between dye molecules and adsorbent [52]. On the other hand, the removal efficiency increased as the adsorbent dosage increased, which was due to the greater availability of active sites on the surface of SPGO3, thus making it easier for the

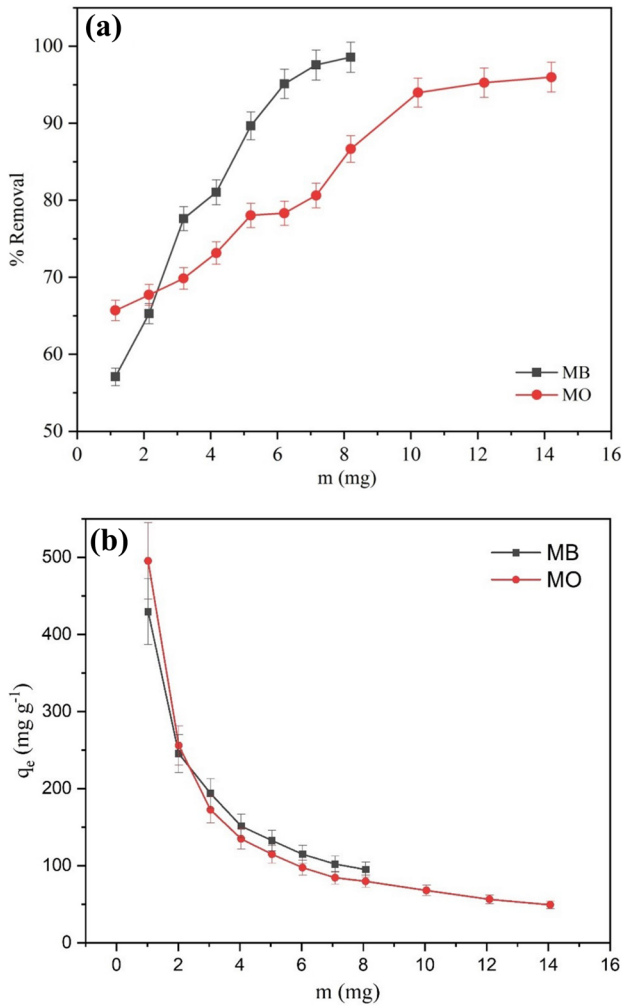

Fig. 10 Effect of adsorbent dosage on **a** Removal of MB and MO dye by SPGO3 nanocomposite and **b** Adsorption capacity for SPGO3 nanocomposite ($c_0 = 30$ mg L^{-1}; V = 25 mL; temperature was 298 K). Error bar = SD (n = 2)

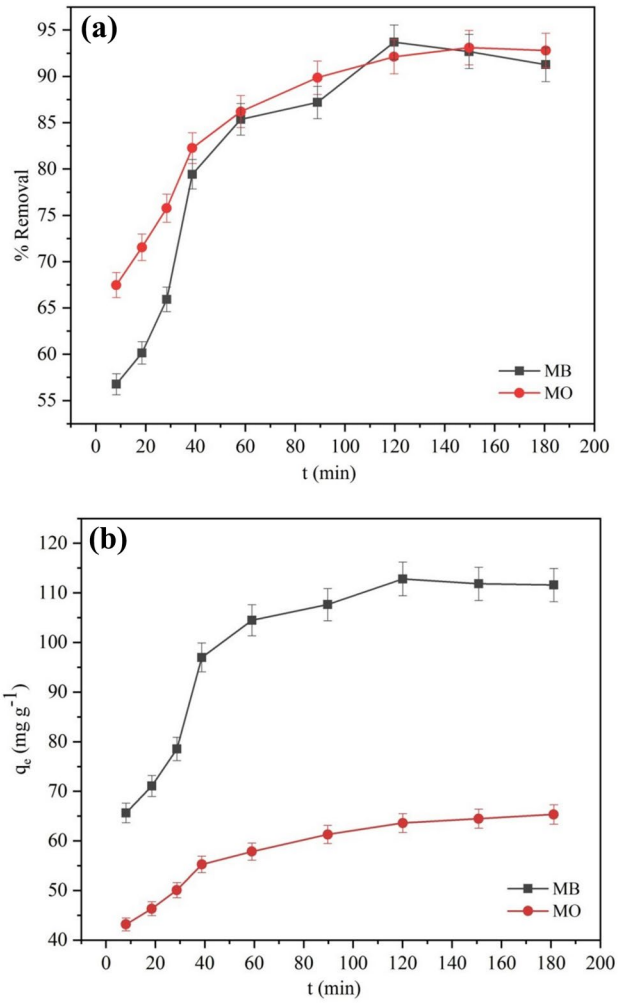

Fig. 11 Effect of contact time on **a** removal of MB and MO dye by SPGO3 nanocomposite and **b** adsorption capacity for SPGO3 nanocomposite ($c_0 = 30$ mg L^{-1}; V = 25 mL; temperature was 298 K) Error bar = SD (n = 2)

dye molecules to enter into the adsorption sites of SPGO3. After a certain point, further increase in dosage resulted in no significant change in removal efficiency. This indicated that higher dosage resulted in saturation of active adsorption sites which in turn inhibited further adsorption of dyes [48]. It was noticed from the results that removal efficiency attained equilibrium at 94% for MB corresponding to 6 mg of SPGO3 dosage and 93% for MO with reference to 10 mg of SPGO3 dosage. Therefore, the optimal adsorbent dosage was fixed at 6 mg for MB and 10 mg for MO in all further experiments.

3.2.3 Effect of contact time

The effect of contact time on the adsorption of MB and MO on the surface of SPGO3 was investigated and its influence on removal efficiency and adsorption capacity are shown in Fig. 11a, b, respectively. The removal efficiency and adsorption capacity increased significantly with increasing contact time was attributed to the presence of a large number of vacant sites on the adsorbent and more available time for the dyes to interact with the vacant sites of the adsorbent. As the adsorption proceeds further, the vacant sites on the surface of SPGO3 became saturated at equilibrium [53]. It was apparent from the figure that, the adsorption of MB and MO on the surface of SPGO3 increased with an increase in time and reached equilibrium at 120 min and 150 min, with approximately 94% and 93% of dye adsorption, respectively. Therefore, the optimal time for adsorption of MB and MO was selected as 120 min and 150 min, respectively, in all further experiments.

3.3 Adsorption kinetics

A kinetic study was carried out to understand the rate-determining step and plausible mechanism of the adsorption process with the help of various kinetic models. Two kinetic models such as pseudo-first-order and pseudo-second-order were used to analyze the data from batch experiments. The pseudo-first-order model is based on the assumption that the adsorption rate is proportional to the quantity of vacant sites. The pseudo-second-order model describes that the adsorption rate is proportional to the square of vacant sites, and chemisorption is the rate-controlling step. The integrated forms of pseudo-first-order and pseudo-second-order equations are as follows [54]:

$$\log\left(q_e - q_t\right) = \log q_e - \frac{k_1}{2.303}t \tag{5}$$

$$\frac{t}{q_t} = \frac{1}{k_2 q_e^2} + \frac{1}{q_e}t \tag{6}$$

where, q_e and q_t are the amount of dye adsorbed (mg g^{-1}) at equilibrium and at time, t (min), respectively, k_1 and k_2 are the rate constant for pseudo-first-order (min^{-1}) and pseudo-second-order (g mg^{-1} min^{-1}) adsorption, respectively.

The linear fitting results of the kinetic data were shown in Fig. 12a, b, and the relevant calculated results are presented in Table 2. As shown in Table 2, the regression (R^2) values of pseudo-second-order adsorption kinetics of the dyes are closer to unity than pseudo-first-order model. The experimentally observed adsorption capacities for MB, 120 mg g^{-1} and MO, 69.5 mg g^{-1} appeared to be closer to that of the calculated values for MB, 124 mg g^{-1} and MO, 73 mg g^{-1} obtained from Eq. 7 which suggests that pseudo-second-order model was appropriate for describing the adsorption process. Thus according to pseudo-second-order assumption, the adsorption of MB and MO dye on SPGO3 is based on chemisorption as the rate-controlling step which involves the exchange or sharing of electrons between the adsorbate and the adsorbent by valence forces [55].

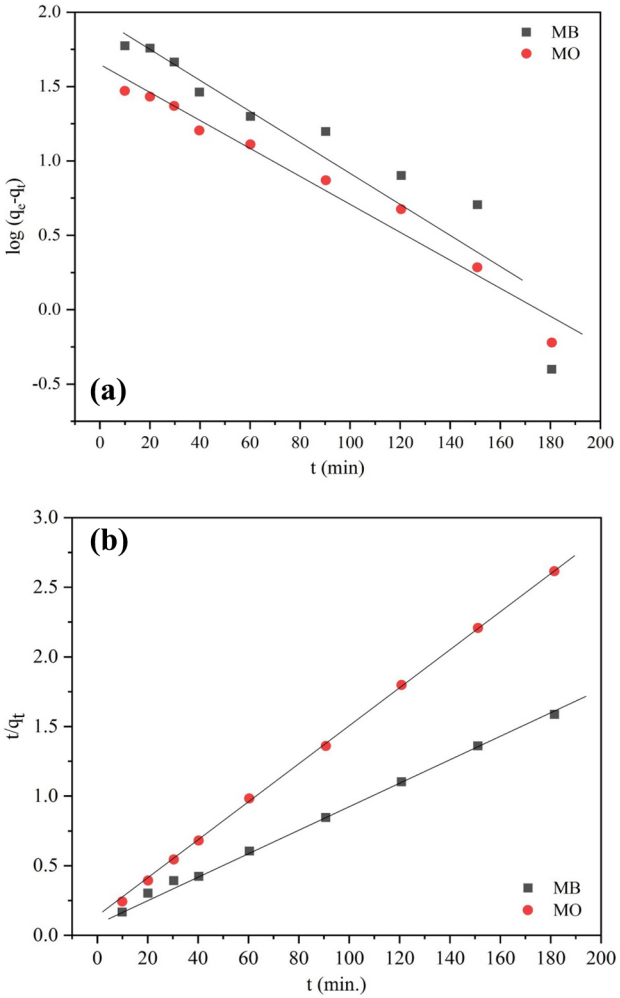

Fig. 12 **a** Pseudo-first-order kinetics, **b** pseudo-second-order kinetics for adsorption of MB (C_0 = 30 mg L^{-1}, pH 8, m/V = 0.24 g L^{-1}, temperature was 298 K) and MO (C_0 = 30 mg L^{-1}, pH 5, m/V = 0.4 g L^{-1}, temperature was 298 K) on SPGO3 nanocomposite

3.4 Adsorption isotherms and thermodynamics

To study the nature of interactions between the adsorbate and adsorbent as well the distribution of adsorbate between the liquid and solid phases at the equilibrium state during the adsorption process, adsorption isotherm experiments were conducted at different temperatures. Two mathematical relations such as Langmuir [56] and Freundlich [57] isotherm models were used and the best fit was found to define the adsorption process at 298 K, 308 K, and 318 K. Langmuir adsorption isotherm describe monolayer adsorption and the

Table 2 Kinetic parameters of pseudo-first-order and pseudo-second-order models for adsorption of MB and MO dyes by SPGO3 nanocomposite

Dye	Pseudo-first-order model				Pseudo-second-order model		
	q_e (exp) (mg g^{-1})	K_1 (min^{-1})	q_e (cal) (mg g^{-1})	R^2	K_2 (mg min g^{-1})	q_e (cal) (mg g^{-1})	R^2
MB	120	0.0137	85	0.8793	0.0007	124	0.9985
MO	69.5	0.0119	31	0.9736	0.0019	73	0.9995

adsorption points being distributed uniformly among the surface of the adsorbent. The adsorbent-adsorbate interaction is believed to be sufficiently strong. Langmuir adsorption isotherm is expressed as:

$$\frac{C_e}{q_e} = \frac{1}{q_m K_L} + \frac{C_e}{q_m} \tag{7}$$

where q_e and c_e are the equilibrium adsorption capacity (mg L^{-1}) and equilibrium concentration (mg L^{-1}), respectively. q_m is the maximum adsorption capacity (mg g^{-1}) and K_L (L mg^{-1}) is the rate constant of Langmuir adsorption isotherm.

Freundlich adsorption isotherm is an empirical relationship used to describe heterogeneous adsorption of the adsorbates at the surface of the adsorbents, resulting to a multilayer coverage. Freundlich adsorption isotherm is expressed as:

$$\ln q_e = \ln K_F + \frac{1}{n} \ln c_e \tag{8}$$

where K_F and n are Freundlich constants reflecting the adsorption capacity and adsorption intensity, respectively. The parameter 'n' reveals whether the adsorption is chemical ($n < 1$) or physical ($n > 1$) in nature.

The results of the isotherm models are presented in Figs. 13 and 14 and the calculated parameters are listed in Table 3. The correlation coefficient (R^2) of Langmuir adsorption model for MB (0.967, 0.965, and 0.975) and MO (0.984, 0.988, and 0.985) at 298 K, 308 K, and 318 K, respectively, yielded more satisfactory results to describe the adsorption process. The maximum adsorption capacity calculated from Langmuir model for MB was 382 mg g^{-1} and MO was 293.3 mg g^{-1} at 298 K. Moreover, the parameter K_L of Langmuir model and n of Freundlich model were both lower than 1, which suggested adsorption was favorable and chemical in nature.

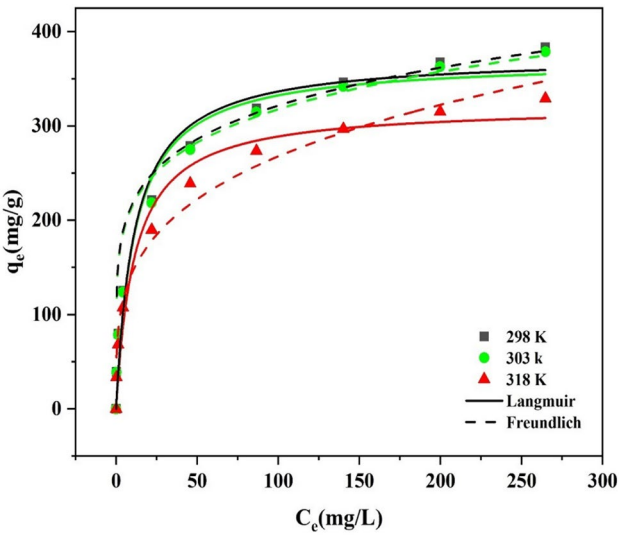

Fig. 13 Langmuir and Freundlich adsorption isotherm fit of MB (5–300 mg L^{-1}, pH 8, m/V = 0.24 g L^{-1}, temperature was 298 K, 308 K and 318 K, and contact time was 120 min) on SPGO3 nanocomposite

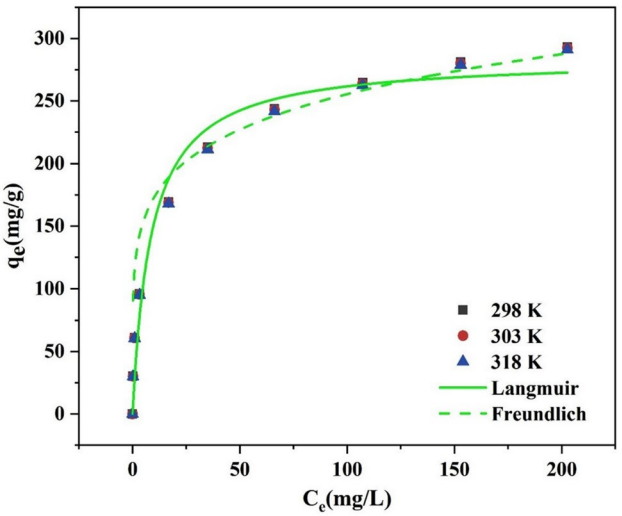

Fig. 14 Langmuir and Freundlich adsorption isotherm fit of MO (C_0 = 10–200 mg L^{-1}, pH 5, m/V = 0.4 g L^{-1}, temperature was 298 K, 308 K and 318 K, contact time was 150 min) on SPGO3 nanocomposite

To study the influence of temperature on the adsorption process, an adsorption experiment was performed at 298 k, 308 K, and 318 K. Thermodynamic parameters such as Gibbs free energy change (ΔG°), enthalpy change (ΔH°), and entropy change (ΔS°) were determined to gain insights in the nature and feasibility of the adsorption process of SPGO3 nanocomposite using the following equations:

$$\ln K_c = \frac{\Delta S^\circ}{R} - \frac{\Delta H^\circ}{RT} \tag{9}$$

$$\Delta G^\circ = \Delta H^\circ - T\Delta S^\circ \tag{10}$$

$$\Delta G^\circ = -RTlnK_c \tag{11}$$

where R (8.314 J mol^{-1} K^{-1}) is gas constant, T (K) is the absolute temperature and K_c is a dimensionless thermodynamic equilibrium constant [58, 59] based on Eq. (11). The calculated thermodynamic parameters are listed in Table 4. The negative values of ΔG° indicated spontaneous nature of the adsorption of MB and MO dye onto SPGO3 nanocomposite. The negative ΔH° values suggested exothermic nature of adsorption process and the negative values of ΔS° described that dye molecules were orderly adsorbed onto the surface of SPGO3 nanocomposite.

Table 3 Adsorption isotherm parameters for adsorption of MB and MO dyes onto SPGO3 nanocomposite

Dye	Temperature (K)	Langmuir isotherm			Freundlich isotherm		
		q_m (mg g^{-1})	K_L (L mg^{-1})	R^2	K_F	1/n	R^2
MB	298	382	0.076	0.967	105	0.219	0.933
	308	377.4	0.063	0.965	73	0.290	0.970
	318	328	0.059	0.975	62	0.293	0.973
MO	298	293.3	0.134	0.984	72	0.285	0.950
	308	292	0.103	0.988	44.7	0.423	0.956
	318	290	0.090	0.985	42	0.426	0.958

Table 4 Thermodynamic parameters for adsorption of MB and MO dyes onto SPGO3 nanocomposite

Dye	ΔH°	ΔS°	ΔG° (KJ mol^{-1})		
	(KJ mol^{-1})	(J K^{-1} mol^{-1})	298 K	308 K	318 K
MB	−16.37	−37.99	−5.13	−4.48	−4.39
MO	−13.72	−31.78	−4.39	−3.69	−3.72

3.5 Effect of ionic strength

The variation of adsorption capacity of MB and MO dyes in presence of K^+, Na^+, Ca^{2+}, and Mg^{2+} are shown in Fig. 15. The effect of ionic strength on MB and MO adsorption onto SPGO3 nanocomposite was investigated using different concentrations of KCl, NaCl, $CaCl_2$, and $MgCl_2$ as the ionic medium. As a consequence of the addition of salts, the generated ionic environment may amplify the shielding of the charge of the dye molecules, which decreases the rate of adsorption [60]. It was seen that the adsorption capacity of SPGO3 nanocomposite declined with an increase in salt concentrations from 50 to 300 mg L^{-1}. The decrease in adsorption capacity may be ascribed to the neutralization of the surface charge of the SPGO3 nanocomposite by electrolyte ions that compete with MB and MO dye molecules for adsorption on the surface of the nanocomposite. However, the decline in adsorption capacity was still acceptable compared to the high removal efficiency of SPGO3 nanocomposite.

3.6 Adsorption mechanism

FT-IR spectroscopy was used to study the interactions between MB and MO dye molecules with the surface of SPGO3 nanocomposite. The spectra of SPGO3 nanocomposite and dye-loaded nanocomposites such as SPGO3-MB and SPGO3-MO were shown in Fig. 16a. The band associated with the stretching vibrations of O–H bonds is located at 3360 cm^{-1} in SPGO3 nanocomposite became weak in the dye-loaded nanocomposites. This suggested that the hydroxyl groups on the surface of SPGO3 nanocomposite were involved in the dye adsorption process. Moreover,

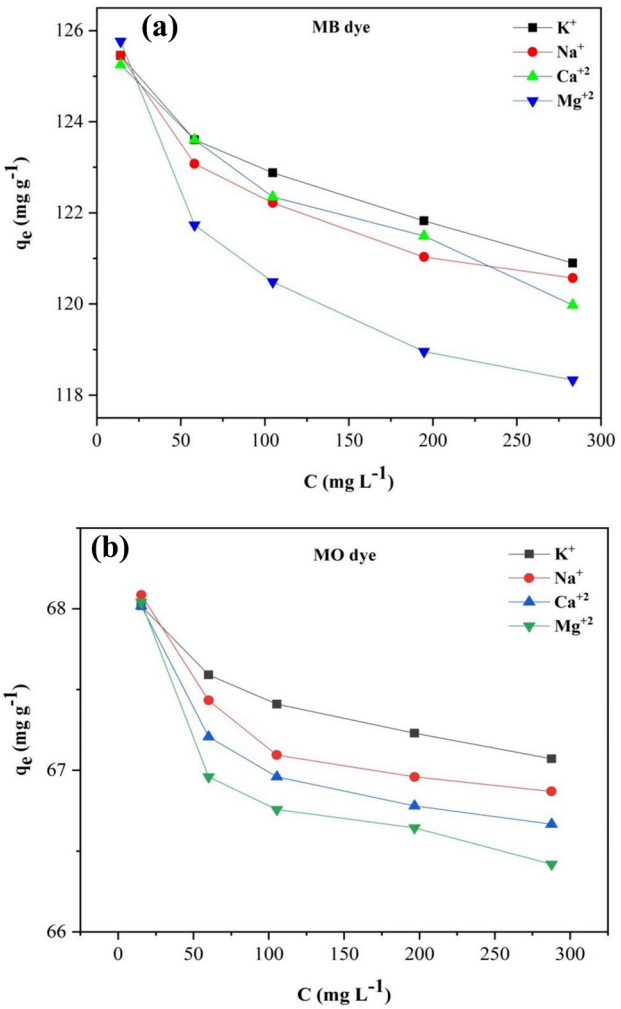

Fig. 15 Effect of ionic strength on adsorption of **a** MB (C_0 = 30 mg L^{-1}, pH 8, m = 6 mg, V = 25 mL, temperature was 298 K and contact time was 120 min) and **b** MO (C_0 = 30 mg L^{-1}, pH 5, m = 10 mg, V = 25 mL, temperature was 298 K and contact time was 150 min)

lone pair of nitrogen atoms in MB and MO dye molecules participate in intermolecular H-bonding with the hydroxyl groups on the surface of SPGO3 nanocomposite [61]. The intensity of the band related to the stretching vibration of C=O bond also decreased in dye-loaded nanocomposites

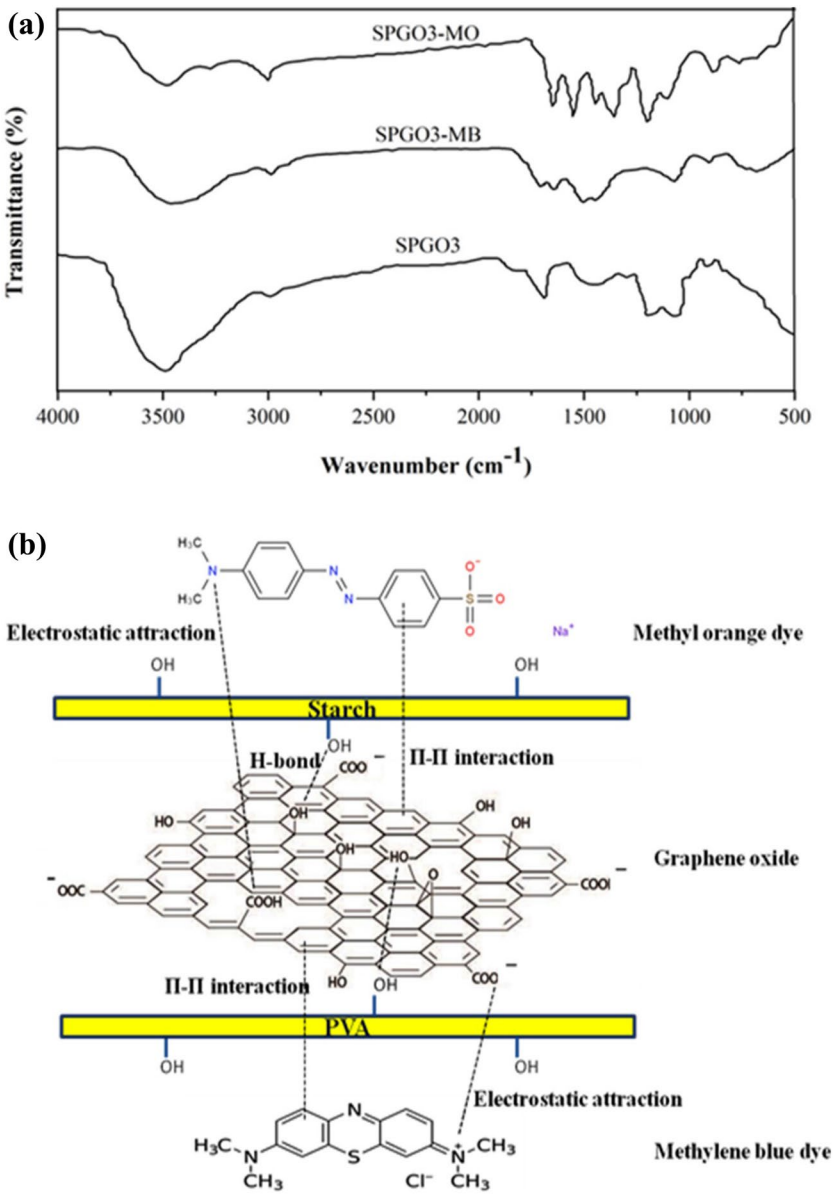

Fig. 16 **a** FT-IR spectra of SPGO3 nanocomposite, SPGO3-MB loaded nanocomposite and SPGO3-MO loaded nanocomposite and **b** possible interactions between the SPGO3 adsorbent and the dye pollutants

indicating that the carbonyl groups take part in electrostatic attraction with the dye molecules [60]. In the SPGO3 nanocomposite, the band related to the C–C stretching vibration in the aromatic ring was located around 1460 cm^{-1}. The intensity of this band decreased in the dye loaded SPGO3 nanocomposites suggesting the existence of Π-Π interaction between the aromatic skeleton of the SPGO3 adsorbent and the aromatic backbone of MB and MO dye molecules [5, 62]. Since the FT-IR spectra showed characteristic shifts in the bands of O–H, C=O and aromatic C–C stretching, we can consider the corresponding locations as possible adsorption sites. Hence, the synergic effects of electrostatic attraction, H-bonding and Π–Π interaction explained the substantial adsorption of MB and MO dye pollutants on the surface of SPGO3 nanocomposite (Fig. 16b).

3.7 Desorption

The potential for regeneration and reusability of an adsorbent is considered for its suitability in commercial applications from an ecological and economic point of view. Therefore, to separate the dye-loaded SPGO3 nanocomposite, 0.1 M HCl solution was used as a desorption medium for MB, and 0.1 M NaOH solution was used as a desorption medium for MO. After centrifugation, the separated SPGO3 nanocomposite was then washed with water and ethanol, in sequence. The nanocomposite was then dried at 35 °C for 72 h and used for the subsequent adsorption–desorption experiments [59]. As shown in Fig. 17, after five times of adsorption–desorption experiments, SPGO3 nanocomposite still exhibited acceptable

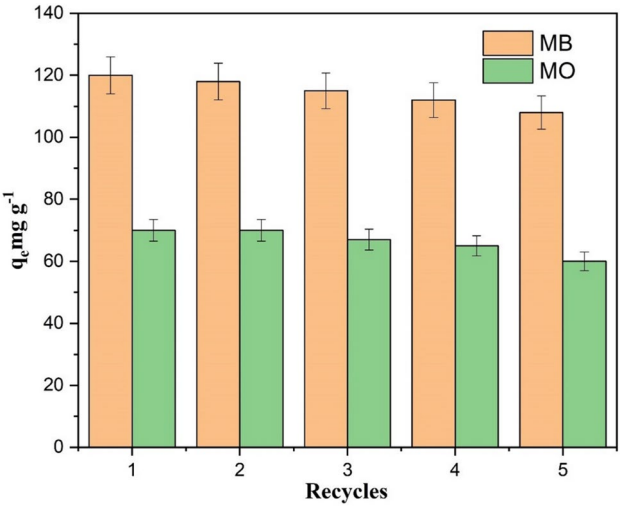

Fig. 17 Adsorption–desorption recycles of **a** MB (C_0 = 30 mg L^{-1}, pH 8, m = 6 mg, V = 25 mL, temperature was 298 K and contact time was 120 min) and **b** MO (C_0 = 30 mg L^{-1}, pH 5, m = 10 mg, V = 25 mL, temperature was 298 K and contact time was 150 min) Error bar = SD (n = 2)

adsorption capacities for MB and MO dyes with low decline.

4 Conclusions

In the present study, GO was introduced as a nanofiller into the starch/PVA polymer matrix to fabricate an efficient adsorbent for the removal of cationic and anionic dyes from the aqueous solution. Due to the incorporation of GO into the starch/PVA matrix, aggregation of GO was prevented, thereby, the performance of SPGO nanocomposites had been greatly improved. The bonds between the GO and starch/PVA polymer included inter- and intra-molecular hydrogen bonds which made these nanocomposites mechanically stronger. The morphological studies showed that GO was homogeneously impregnated onto starch/PVA matrix. The SPGO3 nanocomposite was found to be an effective adsorbent for the removal of MB and MO dyes from the aqueous solution and aided to achieve good adsorption capacity. The SPGO3 nano adsorbent offered a high specific surface area, large pore-size and variable charges on the surface facilitated more active sites for adsorption of pollutants. The kinetic study exhibited that pseudo-second-order model was suitable to explain the adsorption behaviour of SPGO3 nano adsorbent and hence the rate-controlling step could be a chemisorption process. The Langmuir model provided a better correlation with the experimental data suggesting monolayer adsorption. The calculated thermodynamic parameters such as ΔG and ΔH indicated the adsorption process was spontaneous and exothermic, respectively. The mechanism of adsorption was explained based on the synergic effect of electrostatic attraction (based on the surface charge of nano adsorbent), H-bonding (due to the presence of hydrophilic functional groups) and Π-Π interactions (due to the interactions between the aromatic skeleton of SPGO3 nano adsorbent and the aromatic planar dye molecules. These interactions were also validated by FT-IR spectroscopy. The effect of ionic strength on the adsorption capacity of MB and MO dyes in the presence of K^+, Na^+, Ca^{2+}, and Mg^{2+} slightly declined which indicated the nature of electrostatic force for the adsorption process. Therefore, the fabricated SPGO3 nano adsorbent is a promising candidate for the removal of dyes from an aqueous solution.

Acknowledgements The authors are grateful to the management of Auxilium College, Vellore, Tamil Nadu, for providing necessary facilities to the research work.

Author contributions VSP: Resources, methodology, software, writing, editing and visualization. SKB: Validation and reviewing. VSK: Conceptualization, supervision and resources.

Funding No funding was received for the research work.

Availability of data and material The datasets generated during and/or analyzed during the current study are not publicly available due to the ongoing research project but are available from the corresponding author on reasonable request.

Declarations

Conflict of interest The authors declare that they have no known competing financial interests or personal relationships that could have appeared to influence the work reported in this paper.

References

1. Sharma B, Dangi AK, Shukla P (2018) Contemporary enzyme based technologies for bioremediation: a review. J Environ Manag 210:10–22
2. Iqbal M (2016) Vicia faba bioassay for environmental toxicity monitoring: a review. Chemosphere 144:785–802
3. Oliveira SF, da Luz JMR, Kasuya MCM et al (2018) Enzymatic extract containing lignin peroxidase immobilized on carbon nanotubes: potential biocatalyst in dye decolourization. Saudi J Biol Sci 25:651–659

4. Liu C, Liu H, Xu A et al (2017) In situ reduced and assembled three-dimensional graphene aerogel for efficient dye removal. J Alloy Compd 714:522–529
5. Sharma P, Hussain N, Borah DJ, Das MR (2013) Kinetics and adsorption behavior of the methyl blue at the graphene oxide/reduced graphene oxide nanosheet-water interface: a comparative study. J Chem Eng Data 58:3477–3488
6. Ai L, Zhang C, Meng L (2011) Adsorption of methyl orange from aqueous solution on hydrothermal synthesized Mg-Al layered double hydroxide. J Chem Eng Data 56:4217–4225
7. Nassar MY, NourEldien MS, Ibrahim IM, Aly HM (2023) A facile hydrothermal synthesis of S-VO_2-cellulose nanocomposite for photocatalytic degradation of methylene blue dye. Processes 11:1322
8. Guimarães Gusmão KA, Alves Gurgel LV, Sacramento Melo TM, Gil LF (2012) Application of succinylated sugarcane bagasse as adsorbent to remove methylene blue and gentian violet from aqueous solutions—kinetic and equilibrium studies. Dyes Pigm 92:967–974
9. Sharma MK, Sobti RC (2000) Rec effect of certain textile dyes in *Bacillus subtilis*. Mutat Res Genet Toxico Environ Mutagen 465:27–38
10. Akhoondi A, Mirzaei M, Nassar MY et al (2022) New strategies in the preparation of binary g-C_3N_4/MXene composites for visible-light-driven photocatalytic applications. Synth Sinter 2:151–169
11. Aljohani MM, Masoud EM, Mohamed NM, Nassar MY (2021) Cobalt aluminate/carbon nanocomposite via an auto-combustion method: an efficient photocatalyst for photocatalytic degradation of organic dyes from aqueous media. Int J Environ Anal Chem 00:1–21
12. Martínez CM, Celis LB, Cervantes FJ (2013) Immobilized humic substances as redox mediator for the simultaneous removal of phenol and Reactive Red 2 in a UASB reactor. Appl Microbiol Biotechnol 97:9897–9905
13. Zou H, Wang Y (2017) Azo dyes wastewater treatment and simultaneous electricity generation in a novel process of electrolysis cell combined with microbial fuel cell. Bioresour Technol 235:167–175
14. Cheng S, Oatley DL, Williams PM, Wright CJ (2012) Characterisation and application of a novel positively charged nanofiltration membrane for the treatment of textile industry wastewaters. Water Res 46:33–42
15. Xiao D, He M, Liu Y et al (2020) Strong alginate/reduced graphene oxide composite hydrogels with enhanced dye adsorption performance. Polym Bull 77:6609–6623
16. Peng N, Hu D, Zeng J et al (2016) Superabsorbent cellulose-clay nanocomposite hydrogels for highly efficient removal of dye in water. ACS Sustain Chem Eng 4:7217–7224
17. Wu D, Xu H, Hakkarainen M (2016) From starch to polylactide and nano-graphene oxide: fully starch derived high performance composites. RSC Adv 6:54336–54345
18. Aydin AA, Ilberg V (2016) Effect of different polyol-based plasticizers on thermal properties of polyvinyl alcohol:starch blends. Carbohydr Polym 136:441–448
19. Sedaghat E, Rostami AA, Ghaemy M, Rostami A (2019) Characterization, thermal degradation kinetics, and morphological properties of a graphene oxide/poly(vinyl alcohol)/starch nanocomposite. J Therm Anal Calorim 136:759–769
20. Christy PN, Basha SK, Kumari VS (2022) Nano zinc oxide and nano bioactive glass reinforced chitosan/poly(vinyl alcohol) scaffolds for bone tissue engineering application. Mater Today Commun 31:103429
21. Madima N, Mishra SB, Inamuddin I, Mishra AK (2020) Carbon-based nanomaterials for remediation of organic and inorganic pollutants from wastewater. A review. Environ Chem Lett 18:1169–1191
22. Yang K, Wang J, Chen X et al (2018) Application of graphene-based materials in water purification: from the nanoscale to specific devices. Environ Sci Nano 5:1264–1297
23. Ambrosi A, Pumera M (2016) Electrochemically exfoliated graphene and graphene oxide for energy storage and electrochemistry applications. Chem Eur J 22:153–159
24. Abdel-Bary AS, Tolan DA, Nassar MY et al (2020) Chitosan, magnetite, silicon dioxide, and graphene oxide nanocomposites: synthesis, characterization, efficiency as cisplatin drug delivery, and DFT calculations. Int J Biol Macromol 154:621–633
25. Yoo MJ, Park HB (2019) Effect of hydrogen peroxide on properties of graphene oxide in Hummers method. Carbon 141:515–522
26. Huang X, Yin Z, Wu S et al (2011) Graphene-based materials: synthesis, characterization, properties, and applications. Small 7:1876–1902
27. Shanmuga Priya V, Khaleel Basha S, Sugantha Kumari V et al (2019) Facile synthesis of graphene via chemical and biological methods—a review. Int J Pharm Biol Sci 9:336–359
28. Hotan Alsohaimi I, Alhumaimess MS, Abdullah Alqadami A et al (2023) Adsorptive performance of aminonaphthalenesulfonic acid modified magnetic-graphene oxide for methylene blue dye: mechanism, isotherm and thermodynamic studies. Inorg Chem Commun 147:110261
29. Bai H, Chen J, Wang Z et al (2020) Simultaneous removal of organic dyes from aqueous solutions by renewable alginate hybridized with graphene oxide. J Chem Eng Data 65:4443–4451
30. Ma J, Li Y, Yin X et al (2016) Poly(vinyl alcohol)/graphene oxide nanocomposites prepared by: in situ polymerization with enhanced mechanical properties and water vapor barrier properties. RSC Adv 6:49448–49458
31. Hosseinzadeh H, Ramin S (2018) Fabrication of starch-graft-poly(acrylamide)/graphene oxide/hydroxyapatite nanocomposite hydrogel adsorbent for removal of malachite green dye from aqueous solution. Int J Biol Macromol 106:101–115
32. Saeed Alamri M, Hassan HMA, Alhumaimess MS et al (2022) Kinetics and adsorption assessment of 1, 4-dioxane from aqueous solution by thiol and sulfonic acid functionalized titanosilicate. J Mol Liq 362:119786
33. Fakhry H, Hassan HMA, El-Aassar MR et al (2022) A treatment of wastewater containing safranin O using immobilized *Myriophyllum spicatum* L. onto polyacrylonitrile/polyvinylpyrrodlidone biosorbent. J Inorg Organomet Polym Mater 32:3181–3195
34. Nassar MY, Abdallah S (2016) Facile controllable hydrothermal route for a porous $CoMn_2O_4$ nanostructure: synthesis, characterization, and textile dye removal from aqueous media. RSC Adv 6:84050–84067
35. Ahmed A, Niazi MBK, Jahan Z et al (2020) Enhancing the thermal, mechanical and swelling properties of PVA/starch nanocomposite membranes incorporating g-C_3N_4. J Polym Environ 28:100–115
36. Singh N, Riyajuddin S, Ghosh K et al (2019) Chitosan-graphene oxide hydrogels with embedded magnetic iron oxide nanoparticles for dye removal. ACS Appl Nano Mater 2:7379–7392
37. Nassar MY, El-Salhy HI, El-Shiwiny WH et al (2023) Composite nanoarchitectonics of magnetic silicon dioxide-modified chitosan for doxorubicin delivery and in vitro cytotoxicity assay. J Inorg Organomet Polym Mater 33:237–253
38. Refat NM, Nassar MY, Sadeek SA (2022) A controllable one-pot hydrothermal synthesis of spherical cobalt ferrite nanoparticles: synthesis, characterization, and optical properties. RSC Adv 12:25081–25095
39. Ávila-Orta CA, Soriano Corral F, Fonseca-Florido HA et al (2018) Starch-graphene oxide bionanocomposites prepared through melt mixing. J Appl Polym Sci 135:46037
40. Aqlil M, Moussemba Nzenguet A, Essamlali Y et al (2017) Graphene oxide filled lignin/starch polymer bionanocomposite:

structural, physical, and mechanical studies. J Agric Food Chem 65:10571–10581
41. Xu S, Liu J, Xue Y et al (2017) Appropriate conditions for preparing few-layered graphene oxide and reduced graphene oxide. Fuller Nanotubes Carbon Nanostruct 25:40–46
42. Mura S, Jiang Y, Vassalini I et al (2018) graphene oxide/iron oxide nanocomposites for water remediation. ACS Appl Nano Mater 1:6724–6732
43. Lawal IA, Lawal MM, Akpotu SO et al (2020) Noncovalent graphene oxide functionalized with ionic liquid: theoretical, isotherm, kinetics, and regeneration studies on the adsorption of pharmaceuticals. Ind Eng Chem Res 59:4945–4957
44. Biru I, Damian CM, Gârea SA, Iovu H (2016) Benzoxazine-functionalized graphene oxide for synthesis of new nanocomposites. Eur Polym J 83:244–255
45. Islam MR, Mollik SI (2020) Enhanced electrochemical performance of flexible and eco-friendly starch/graphene oxide nanocomposite. Heliyon 6:e05292
46. Shi H, Li W, Zhong L, Xu C (2014) Methylene blue adsorption from aqueous solution by magnetic cellulose/graphene oxide composite: equilibrium, kinetics, and thermodynamics. Ind Eng Chem Res 53:1108–1118
47. Konwar A, Kalita S, Kotoky J, Chowdhury D (2016) Chitosan-iron oxide coated graphene oxide nanocomposite hydrogel: a robust and soft antimicrobial biofilm. ACS Appl Mater Interfaces 8:20625–20634
48. Cui L, Wang Y, Hu L et al (2015) Mechanism of Pb(II) and methylene blue adsorption onto magnetic carbonate hydroxyapatite/graphene oxide. RSC Adv 5:9759–9770
49. Kamal MA, Bibi S, Bokhari SW et al (2017) Synthesis and adsorptive characteristics of novel chitosan/graphene oxide nanocomposite for dye uptake. React Funct Polym 110:21–29
50. Poonguzhali R, Basha SK, Kumari VS (2017) Synthesis and characterization of chitosan/poly(vinylpyrrolidone) biocomposite for biomedical application. Polym Bull 74:2185–2201
51. Jsc E, Gopi S, A R, et al (2019) Highly crosslinked 3-D hydrogels based on graphene oxide for enhanced remediation of multi contaminant wastewater. J Water Process Eng 31:100850
52. Pourjavadi A, Nazari M, Kabiri B et al (2016) Preparation of porous graphene oxide/hydrogel nanocomposites and their ability for efficient adsorption of methylene blue. RSC Adv 6:10430–10437
53. Ma YX, Shao WJ, Sun W et al (2018) One-step fabrication of β-cyclodextrin modified magnetic graphene oxide nanohybrids for adsorption of Pb(II), Cu(II) and methylene blue in aqueous solutions. Appl Surf Sci 459:544–553
54. Al Subhi A, Valizadeh Kiamahalleh M, Firouzi M et al (2020) Self-assembled graphene hydrogel composites for selective dye removal. Adv Sustain Syst 4:2000055
55. Gopalakrishnan A, Singh SP, Badhulika S (2020) Reusable, few-layered-MoS_2 nanosheets/graphene hybrid on cellulose paper for superior adsorption of methylene blue dye. New J Chem 44:5489–5500
56. Ma Z, Liu D, Zhu Y et al (2016) Graphene oxide/chitin nanofibril composite foams as column adsorbents for aqueous pollutants. Carbohydr Polym 144:230–237
57. Liu Y, Huang S, Zhao X, Zhang Y (2018) Fabrication of three-dimensional porous β-cyclodextrin/chitosan functionalized graphene oxide hydrogel for methylene blue removal from aqueous solution. Colloids Surf A 539:1–10
58. Nassar MY, Ali EI, Zakaria ES (2017) Tunable auto-combustion preparation of TiO_2 nanostructures as efficient adsorbents for the removal of an anionic textile dye. RSC Adv 7:8034–8050
59. Nassar MY, Ahmed IS, Raya MA (2019) A facile and tunable approach for synthesis of pure silica nanostructures from rice husk for the removal of ciprofloxacin drug from polluted aqueous solutions. J Mol Liq 282:251–263
60. Bhattacharyya A, Banerjee B, Ghorai S et al (2018) Development of an auto-phase separable and reusable graphene oxide-potato starch based cross-linked bio-composite adsorbent for removal of methylene blue dye. Int J Biol Macromol 116:1037–1048
61. Sharma P, Das MR (2013) Removal of a cationic dye from aqueous solution using graphene oxide nanosheets: investigation of adsorption parameters. J Chem Eng Data 58:151–158
62. Shahabuddin S, Sarih NM, Kamboh MA et al (2016) Synthesis of polyaniline-coated graphene oxide@$SrTiO_3$ nanocube nanocomposites for enhanced removal of carcinogenic dyes from aqueous solution. Polymers 8:305